Behavior of the ionosphere and thermosphere subject to extreme solar cycle conditions

C. G. Smithtro[1] and J. J. Sojka

Center for Atmospheric and Space Sciences, Utah State University, Logan, Utah, USA

Received 8 September 2004; revised 21 March 2005; accepted 2 June 2005; published 18 August 2005.

[1] A 1-D global average ionosphere and thermosphere (GAIT) model is used to examine the climatological behavior of the upper atmosphere, subject to both extremely low and high solar flux. These extremes are justified, in part, by the Maunder Minimum and Grand Maximum epochs described by J. A. Eddy, as well as other studies involving cosmogenic isotopes and Sun-like stars. As the irradiance falls below normal solar minimum levels, the concentration of O^+ decreases rapidly relative to the molecular ions, such that the ratio f_oF_2/f_oF_1 approaches unity. When subject to exceptionally high solar fluxes, the ionospheric peak electron density (N_mF_2) unexpectedly plateaus, remaining relatively constant even as the photon flux continues to increase. In both cases, the state of the underlying thermosphere, particularly the neutral gas temperature, is found to be largely responsible. Model trends are discussed in relation to ionospheric observations, specifically the preponderance of so-called ionospheric G conditions at solar minimum and f_oF_2 saturation at solar maximum, as well as the problem of Earth's global helium budget.

Citation: Smithtro, C. G., and J. J. Sojka (2005), Behavior of the ionosphere and thermosphere subject to extreme solar cycle conditions, *J. Geophys. Res.*, *110*, A08306, doi:10.1029/2004JA010782.

1. Introduction

[2] An examination of the historical sunspot record reveals an extended period, between 1645 and 1715 A.D., during which time virtually no sunspots were observed. This period is now known as the Maunder Minimum. Independent evidence from studies of cosmogenic isotopes [*Eddy*, 1976; *Webber and Higbie*, 2003] and Sun-like stars [*Baliunas and Jastrow*, 1990; *White et al.*, 1992; *Lean et al.*, 2001] suggests that solar activity during this time was markedly lower than contemporary levels.

[3] Using historical sunspot and aurora sightings, as well as a reconstruction of the cosmogenic isotope ^{14}C, *Eddy* [1976] also identified a period of intense solar activity, between roughly 1100 and 1250 A.D., which he termed the Grand Maximum. Although a recent reexamination of the ^{14}C record [*Solanki et al.*, 2004] casts some doubt on the magnitude of the Grand Maximum, the longer-term ^{14}C record suggests the Sun has undergone periods of extremely active conditions, higher than contemporary maximum.

[4] The occurrence of such solar activity extremes would imply corresponding decreases or increases in ultraviolet emissions from the Sun's chromosphere and corona, directly affecting the characteristics of the Earth's thermosphere and ionosphere. The goal of the present work is to describe the response of the ionosphere and thermosphere to these hypothetical extremes using plausible representations of the solar irradiance, specifically the range 3–360 nm. This effort constitutes the second in a series of two papers that examine the response of the upper atmosphere to the input solar irradiance. In the first paper, *Smithtro and Sojka* [2005, hereinafter referred to as paper 1] developed the model needed for such an exploration.

[5] Paper 1 describes a 1-D global average ionosphere and thermosphere (GAIT) model built specifically to explore irradiance inputs outside the range of the normal solar cycle. R.G. Roble and others first developed the global average concept as a stepping stone toward full 3-D global circulation models, and found they could reproduce the climatological behavior of the upper atmosphere [*Roble and Emery*, 1983; *Roble et al.*, 1987; *Roble*, 1995]. The 1-D GAIT model neglects horizontal and diurnal variations, but does provide a physically realistic picture of how an idealized atmosphere responds to solar input. Sophisticated 3-D models paint a more complete picture, but are much more complex, have exponentially greater computational requirements, and are more difficult to interpret. Given the speculative and preliminary nature of this work, we posit that a 1-D global average model is better suited to the task at hand.

[6] In this paper, we first expand upon the motivation for studying extremely low and high solar activity levels. We next describe our approach for extrapolating the solar irradiance. A brief discussion of the GAIT model follows, including a description of modifications made subsequent

[1]Now at Air Force Institute of Technology, Wright-Patterson Air Force Base, Ohio, USA.

0148-0227/05/2004JA010782$09.00

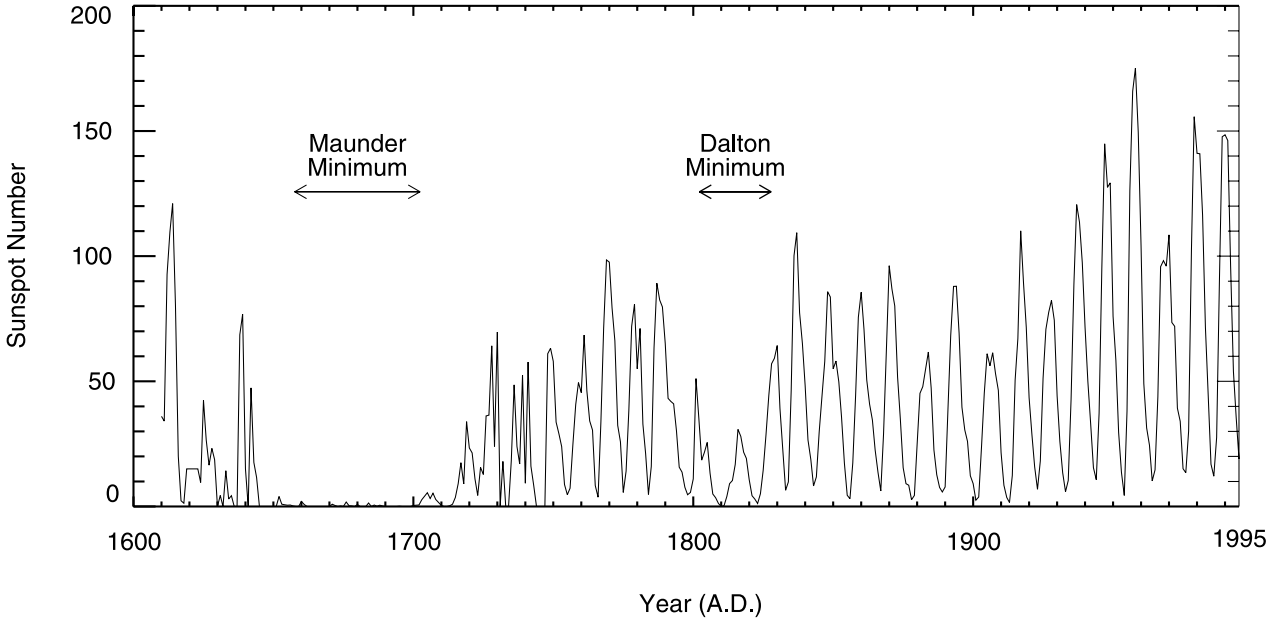

Figure 1. A time series of the mean annual group sunspot number is shown, covering the period 1610–1995 A.D. [*Hoyt and Schatten*, 1998a, 1998b].

to paper 1. Finally, we present GAIT model results representing both a systematic decrease of the solar irradiance toward Maunder Minimum type levels as well as an increase of the irradiance to three times the normal solar cycle variation. Obviously the model output of such extreme conditions cannot be directly compared to observations; however, we can use the predicted trends to describe behavior observed at the limits of the normal solar cycle.

2. Motivation

[7] *Hoyt and Schatten* [1998a, 1998b] reviewed the available sunspot records and constructed an internally self-consistent time series of the sunspot group number that extends back to 1610 A.D. Figure 1 displays the annual mean of this group number from 1610 to 1995 A.D. Virtually no sunspots were observed during the extended period from roughly 1645 to 1715 A.D., now known as the Maunder Minimum [*Eddy*, 1976]. From roughly 1800 to 1830 A.D., the sunspot counts were again low and the cycle lengthened; it has even been suggested the Sun skipped a cycle during this so-called Dalton Minimum [*Usoskin et al.*, 2001]. Earlier, less reliable sunspot records, hint at other minima between 600 and 800 A.D. (the Medieval Minimum) and 1460 and 1550 A.D. (the Spörer Minimum) [*Wittmann and Xu*, 1987], as well as a Grand Maximum between 1100 and 1250 A.D. [*Eddy*, 1976].

[8] One might assume the low sunspot number observed during Maunder Minimum represented merely an extended solar minimum, and thus expect the solar irradiance during that time to be similar to contemporary solar minima. However, additional, independent lines of evidence suggest the Maunder Minimum irradiance was in fact dramatically different. Cosmogenic isotopes such as ^{14}C and ^{10}Be are formed via the interaction between cosmic ray protons and the Earth's atmosphere. Long-term records of the ^{10}Be production rate can be inferred through analysis of ice cores [*Webber and Higbie*, 2003], and in the case of ^{14}C, tree rings [*Eddy*, 1976]. After accounting for slow changes in the Earth's geomagnetic field, modulation of the heliospheric magnetic field is the dominant source of variability in the galactic cosmic ray flux reaching the Earth. Both the strength of the heliospheric magnetic field and the Sun's coronal and chromospheric emission are related through their dependence on the emergence of magnetic flux in the solar atmosphere. Analysis of the cosmogenic isotope record thus provides an independent measure of the level of solar activity, and can be used to infer the Sun's irradiance.

[9] *Webber and Higbie* [2003] recently reported on the systematic variation of ^{10}Be production extending back through the Maunder Minimum period. They found the normal 11-year solar cycle modulation of cosmic rays to result in production rates that are roughly a factor of 1.5–2.0 larger at solar minimum than maximum. The ^{10}Be production rate calculated during the Maunder Minimum epoch was even higher than contemporary minima, by a factor of 1.8–2.0, consistent with negligible solar modulation of the cosmic rays. *Eddy* [1976] found a similarly large difference between the contemporary ^{14}C production rate and that during the Maunder Minimum epoch. Given the correlation between cosmogenic isotope production and the solar cycle, this suggests the solar irradiance during Maunder Minimum, particularly coronal emissions, would be significantly reduced below "normal" minimum levels. It should be noted that the interpretation of such long-term records is nontrivial. Not only is there a general uncertainty in fitting a geomagnetic mean curve to the isotope data, but short-term changes in Earth's magnetic moment also affect the results.

[10] A second line of evidence involves astronomical measurements of Sun-like stars. Chromospheric emissions from Sun-like stars exhibit a broad range of variability, with average irradiance values both higher and lower than is seen

in the contemporary Sun [*Baliunas and Jastrow*, 1990; *White et al.*, 1992; *Radick et al.*, 1998; *Radick*, 2003]. Roughly 20% of these stars undergo little to no cyclic variation, and their average chromospheric emission levels are correspondingly lower than the others [*Radick*, 2003]. *Lean et al.* [2001] suggested these noncycling stars could be analogs to the Sun's behavior during Maunder Minimum, and used that assumption to estimate the requisite change in the Sun's chromospheric emission during that epoch.

[11] Using the sunspot group number as a proxy, *Lean et al.* [2001] constructed a solar chromospheric activity index extending back through 1610 A.D. When based on the sunspot number alone, the emission distribution of their index mimicked only the upper end of the Sun-like star distribution, and during the Maunder Minimum epoch failed to generate the lower emissions expected of a noncycling star [*Baliunas and Jastrow*, 1990]. However, by including a background component that varied according to the 15-year average sunspot number, their reconstructed distribution better approximated the full range of Sun-like stars, including the Maunder Minimum analogues. Over the course of a typical modern solar cycle, the Lean et al. index increased by roughly a factor of 1.2; while from Maunder Minimum to modern minima the predicted increase was an additional factor of $\sim$1.2. Taken together with the variation in cosmogenic isotopes, these results lead to the conclusion that solar emissions during the Maunder Minimum were dramatically lower than modern minima. Furthermore, the long-term ^{14}C record indicates that the Maunder Minimum was in no way an isolated event.

[12] Cosmogenic isotopes and Sun-like stars also provide evidence for periods of extremely high solar activity. As mentioned previously, *Eddy* [1976] used the ^{14}C record as well as the frequency of naked eye sunspot observations and aurora sightings to identify a period of enhanced solar activity from 1100 to 1250 A.D., which he termed the Grand Maximum. A new analysis of the ^{14}C and ^{10}Be records by *Solanki et al.* [2004] discounts the strength of Eddy's Grand Maximum, but continues to indicate episodes of extreme solar modulation over the long-term isotope record.

[13] The Sun-like star distribution similarly suggests the possibility of much higher emission levels; fully two thirds of the stars in the sample exceed the average chromospheric emission level of the Sun [*Radick et al.*, 1998]. Studies of Sun-like stars thus lend credence to the idea that the Sun is capable of a much wider range of activity than has been observed in the modern era. With that as motivation, we set out to explore the climatological behavior of the Earth's thermosphere and ionosphere subject to solar irradiance well outside the range of the normal solar cycle.

3. Solar Irradiance

[14] We frequently quantify the solar cycle progression in terms of a physical measure such as the 10.7 cm radio flux (F10.7). However, earlier work has exposed a breakdown in the desired linear relationship between this proxy and the actual solar irradiance for high F10.7 [*Balan et al.*, 1994a, 1994b; *Richards et al.*, 1994]. *Richards et al.* [1994] argued the nonlinear behavior could be largely removed by supplementing the daily F10.7 with its 81-day running average to create a new proxy, P, where $P = (F10.7 + \langle F10.7 \rangle_{81})/2$.

[15] On the basis of the earlier work of *Lean et al.* [2001], J. L. Lean (private communication, 2004) suggested a reasonable representation of the Maunder Minimum irradiance could be obtained by reducing the normal solar minimum flux by an amount equal to the typical solar cycle increase; a more conservative estimate reduces the flux by only half that amount. Under these assumptions Maunder Minimum conditions would be represented by P between -10 and -90, where the negative values again reflect nonlinearity of the underlying F10.7 proxy. To avoid confusion regarding the meaning of such negative values, we instead adopt a new index that has no physical connotations.

[16] We define a solar cycle factor, S, in which S = 0 identifies normal solar minimum and S = 1 solar maximum. We assume S = 0 corresponds to approximately P = 70, and similarly S = 1 to P = 230. On the basis of the recommendation of J. L. Lean, Maunder Minimum resides somewhere between S = -0.5 and S = -1. It is not our intention to identify the "true" Maunder Minimum irradiance; rather, we will explore the behavior of the ionosphere and thermosphere over a range of activity levels, using S = -1 as a lower limit.

[17] Our motivation also indicated that higher levels of solar activity are possible, but otherwise gave little guidance for an absolute upper limit. Rather than attempt to justify a particular S value as an upper limit, we instead chose to explore a range based on the behavior of the ionosphere. By using an upper limit of S = 3, we are able to capture a distinct morphology, particularly within the ionosphere, without severely disrupting any of the model's physical assumptions.

[18] In terms of S, linear extrapolation of the solar irradiance at a given wavelength is specified by

$$I[\lambda] = I_{S=0}[\lambda]((\mathrm{var}[\lambda] - 1)\mathrm{S} + 1) \quad (1)$$

where λ is the wavelength of interest, $I_{S=0}$ the solar minimum flux, and var[λ] the ratio of the solar maximum to minimum flux, which we term the variability factor. Note, when S equals zero and one, we recover the solar minimum and maximum values respectively.

[19] Equation (1) describes the framework for extrapolating the solar irradiance, the actual representation we used is based on the vacuum ultraviolet (VUV) irradiance model [*Woods and Rottman*, 2002] as shown in Figure 2. Further details concerning the VUV model and how it is implemented in the GAIT model can be found in paper 1. Figure 2 (top) shows the VUV solar minimum reference spectrum (S = 0) as well as two extrapolated spectra, corresponding to both the upper (S = 3) and lower (S = -1) limits explored in this work. Figure 2 (bottom) details the variability factor introduced above. As depicted in Figure 2, wavelengths less than $\sim$40 nm, which originate primarily in the solar corona, have the highest variability. The longer wavelengths originate lower in the solar atmosphere and have correspondingly lower variability. A dotted line in Figure 2 (bottom) delineates those wavelengths with a variability factor greater than 2; per equation (1), the photon

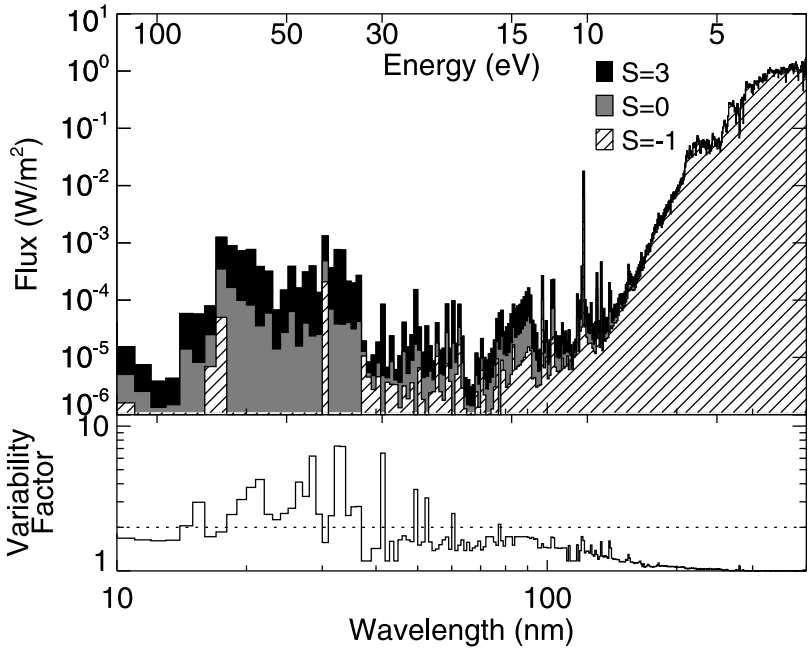

Figure 2. VUV irradiance model [*Woods and Rottman*, 2002] used to specify the solar irradiance. (top) The solar minimum reference spectrum (S = 0) as well as extrapolated spectra representing hypothetical Maunder Minimum (S = −1) and extreme solar maximum (S = 3) conditions are shown. (bottom) A variability factor, defined as the ratio of the solar maximum to minimum flux, is detailed. A dotted line delineates wavelengths with a variability factor greater than 2; per linear extrapolation, the photon flux in these bins decreases to zero by S = −1.

flux in these bins is negative at S = −1. Obviously, negative fluxes are unphysical and must be set to zero in the model, but the result implies that the highly variable coronal emissions are negligible at S = −1. The irradiance at these low S values is then dominated by appropriately reduced chromospheric and photospheric emissions.

3.1. Extrapolation to Extreme Solar Minimum

[20] The fact that linear extrapolation to S = −1 produces zero flux for many short wavelengths is not a physically satisfying result. Even if the coronal emission goes to zero, underlying emission should still remain. The problem is that highly variable coronal lines dominate the flux at these short wavelengths, and this variability drives the entire bin negative during extrapolation. A quick check of the blackbody irradiance at these wavelengths shows the contribution from the underlying photospheric continuum is negligible; however, since variability in the chromosphere is much less than the corona, chromospheric emissions should still remain.

[21] To generate a more accurate estimate of the irradiance, we could separate the coronal and chromospheric emissions prior to extrapolation. This "component" approach requires high spectral resolution, 1-Å or better. In addition, we should scale the chromospheric line and continuum emission separately, since they too exhibit different solar cycle variability. Unfortunately, the VUV irradiance model has neither the requisite spectral resolution, nor any provision to separate line from continuum emission.

[22] The semiphysical NRLEUV irradiance model [*Warren et al.*, 2001] is capable of separating coronal and chromospheric emissions, and would be ideal for creating a Maunder Minimum type spectrum. However, the dynamic range of the NRLEUV model is much less than other irradiance models [*Lean et al.*, 2003], and, when used with the GAIT model, it cannot reproduce the expected solar cycle variation in the neutral gas exospheric temperature [*Smithtro and Sojka*, 2005]. These problems preclude us from using NRLEUV as a standard input to the GAIT model. However, for the sake of a sensitivity analysis, we briefly employ the NRLEUV model in order to compare high- and low-resolution representations of the irradiance as the solar cycle factor approaches S = −1.

[23] We created input spectra using the NRLEUV irradiance model, at both high (1-Å) and low (1-nm) resolution. For the high-resolution representation, the line and continuum contributions were scaled separately, combined, and then rebinned on a 1-nm grid. In the low-resolution approach we simply extrapolated the 1-nm spectrum using equation (1). Comparing the two spectra for S = −1, the high-resolution approach resulted in a 19% greater EUV energy flux, while at S = −0.5 the difference was only 11%; the acronym EUV is used to identify wavelengths between 3 and 105 nm. At the longer ultraviolet wavelengths there is no difference between the high- and low-resolution approaches.

[24] The sensitivity of the coupled ionosphere and thermosphere to these two spectra was gauged using the GAIT model. The modeled total electron content (TEC) differed by less than 19% between the low- and high-resolution approaches, and there was less than a 3% difference in the modeled exospheric temperature. These differences are relatively small, especially when weighed against the inherent uncertainty involved in linearly extrapolating the vari-

Table 1. Solar Energy Flux (W/m^2) as a Function of the Activity Index S, in Six Wavelength Bands, Calculated Using the VUV Irradiance Model [*Woods and Rottman*, 2002][a]

	Solar Energy Flux, W/m^2					
S	3–105 nm	121.6 nm	125–175 nm	175–200 nm	200–360 nm	Total
−1	6.09E-4	2.14E-3	1.19E-2	4.58E-2	6.58E+1	6.59E+1
0	3.02E-3	6.19E-3	1.36E-2	5.00E-2	6.60E+1	6.61E+1
1	6.90E-3	1.02E-2	1.54E-2	5.42E-2	6.62E+1	6.64E+1
2	1.08E-2	1.43E-2	1.71E-2	5.85E-2	6.65E+1	6.66E+1
3	1.47E-2	1.84E-2	1.88E-2	6.27E-2	6.68E+1	6.69E+1
	0.03%	65%	5%	70%	100%	100%

[a]The percentage of energy penetrating through to the mesosphere is given in the bottom row.

ous emission components to S = −1. More important for our later discussion, a comparison of the various neutral and ion gas concentrations showed no significant phenomological differences between the high- and low-resolution approaches. Given these results, it appears we can reasonably neglect the underlying chromospheric emissions, and allow wavelength bins dominated by coronal flux to go to zero as S → −1. We therefore revert to the 1-nm resolution VUV model for the remainder of this work, but address this issue again in section 6.2.

3.2. Solar Energy Input

[25] It is important to note that even though there are large differences between the normal (S = 0) and extreme spectra shown in Figure 2, the total energy input to the atmosphere is essentially unchanged. Tracking the total solar energy input is important because we assume the lower boundary conditions remain constant over the range S = −1 to 3. One way to gauge the impact to the lower atmosphere is by considering the flux of solar energy penetrating through to the mesosphere. Table 1 lists the solar energy flux, at the top of the atmosphere, in six wavelength bins, and for five different values of S. The bottom row of the table gives the percentage of this incident energy that penetrates through to the mesosphere. As it turns out, this percentage is effectively independent of S for each wavelength bin.

[26] In the EUV (3–105 nm), the energy flux increases by nearly a factor of 25 between S = −1 and 3, but it is deposited almost exclusively in the thermosphere; only 0.03% of this flux penetrates to the mesosphere. At longer wavelengths, a greater fraction of the energy penetrates, but the variability is smaller. Because the photon flux increases exponentially with wavelength, the integrated 3–360 nm energy flux is dominated by the longest wavelength bin (200–360 nm). Effectively all of this energy passes through to the mesosphere, but between S = −1 and 3 the total energy flux increases by less than 2%. The relative invariance of the total energy input helps to justify our assumption that the lower boundary conditions are approximately constant over the range S = −1 to 3. Certainly there would be some differences in the properties of the mesopause over the entire range, but extrapolating from the normal solar cycle variation we estimate they should be less than 10%.

4. GAIT Model

[27] The concept of a 1-D global average model was pioneered by R.G. Roble and others as a means of understanding the climatological behavior of the upper atmosphere [*Roble and Emery*, 1983; *Roble et al.*, 1987; *Roble*, 1995]. The 1-D GAIT model used in this work builds on that foundation, and is thoroughly described in paper 1. Given the long time constants of the thermosphere, the GAIT modeled temperature and neutral gas concentrations are reasonably representative of the average conditions, since these parameters undergo relatively little diurnal variation. On the other hand, time constants in the ionosphere are shorter, and there is typically a strong diurnal variation in the electron density and plasma temperature. The concept of a globally averaged ionosphere is therefore not as intuitive. Because the solar input is ever-present, yet reduced by averaging, it is more appropriate to think of the ionosphere calculated by the GAIT model as representing midlatitude daytime conditions, subject to the underlying modeled thermosphere. Indeed, ion concentrations calculated by the GAIT model are very similar to midlatitude daytime results from 3-D physical models, such as the Time-Dependent Ionosphere Model [*Schunk*, 1988].

[28] Since the goal of this work is to explore the upper atmosphere's response to irradiance inputs outside of the normal solar cycle, the GAIT model is built to be largely independent of a specific solar irradiance representation. For example, rather than using volume heating rates parameterized by F10.7 or some other proxy, the model directly accounts for the photon flux between 3 and 360 nm. The GAIT model also includes an approximate treatment of photoelectrons, rather than relying on simple scale factors of secondary ionization or parameterizations of the thermal electron volume heating rate.

[29] To further the model's independence from solar proxies, one change is made to the description given in paper 1. Downward heat flux sets the upper boundary condition for the electron gas temperature, and in paper 1 this was condition was specified by a parameterization based on F10.7. As described in the previous section, the assumed Maunder Minimum irradiance is represented by negative values of F10.7, and under these conditions the parameterized boundary condition breaks down. In an updated version of GAIT used in this work, the heat flux boundary condition is instead tied to the photoelectron energy flux, which is calculated self-consistently within the model. This approach assumes the majority of the heat flux comes from the conjugate hemisphere rather than the magnetosphere. At the upper boundary, the heat flux is set equal to 1/10th of the photoelectron energy flux calculated at a pressure of 2.5 μPa, which is the highest level that the photoelectron flux is calculated (see paper 1 for details). Over the normal solar cycle range, this approximation reproduces the original parameterization to within 10%,

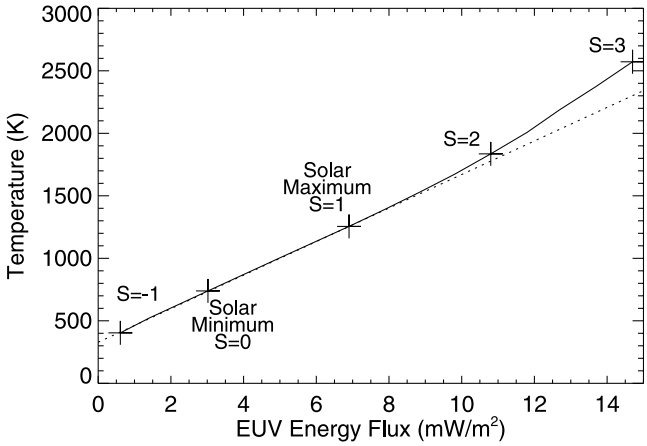

Figure 3. Variation of the global mean exospheric temperature, shown as a function of the input EUV energy flux. The solid line corresponds to GAIT model results; crosses identify the location of integer S values. The dotted line corresponds to a linear fit over the normal solar cycle and is extrapolated over the entire range to highlight deviations from linearity.

with the added benefit that the boundary condition is now self-consistent with the input solar spectrum.

[30] The model's lower boundary is set to 95 km, coinciding with the height of the global average mesopause. The temperature at this boundary is fixed at 177 K, on the basis of a global average obtained from the empirical Mass Spectrometer Incoherent Scatter (MSIS-90) model [*Hedin*, 1991]. At this altitude, the MSIS-90 global average temperature varies less than 1% over the course of the normal solar cycle, and we assume similarly small changes would occur subject to the conditions imposed here. The N_2 and O_2 boundary conditions are similarly held fixed, again on the basis of MSIS-90 global averages. Later we describe the sensitivity of the results to changes in these boundary conditions 6.1. The complete set of boundary conditions is described in paper 1.

5. Model Results

[31] The GAIT model was run using an S index ranging from S = −1 to S = 3. All other inputs were held constant, including a Joule heating term (Q_{Joule}) that adds a fixed 70 GW to the global energy input [*Roble et al.*, 1987; *Smithtro and Sojka*, 2005]. At S = 1, Q_{Joule} accounts for roughly 5% of the total energy input to the model; as the photon flux decreases, the relative contribution rises, reaching 8% by S = −1. Conversely, the relative contribution falls to 3% at S = 3. Lacking a concomitant model of the solar wind and magnetosphere, we are unable to self-consistently vary Q_{Joule} with S, and chose instead to keep it fixed. Barring an unforeseen dramatic change in Q_{Joule}, this assumption has only a small impact on the conclusions that follow.

5.1. Thermospheric Response

[32] Figure 3 presents model calculations of the global mean neutral gas exospheric temperature as a function of the input EUV energy flux. In Figure 3, crosses identify integer values of S over the range S = −1 to 3. On the basis of the extrapolation described by equation (1), the input energy flux increases linearly from S = 0 to 3, and therefore these crosses are evenly spaced. However, as S decreases toward S = −1 the flux in individual wavelength bins goes to zero and can no longer decrease, disrupting the linear relationship.

[33] In paper 1, we showed that the modeled exospheric temperature responds nearly linearly to the input EUV energy flux over the course of the normal solar cycle; this behavior is again seen in Figure 3. The solid line corresponds to the model results, while the dotted line represents an extrapolation of the linear behavior observed between S = 0 and 1. The global mean exospheric temperature is calculated to be 1255 K at solar maximum and 739 K at solar minimum, in close agreement with global average MSIS-90 results [*Smithtro and Sojka*, 2005]. For S < 0, the temperature continues to follow the linear trend. As S increases, the response remains roughly linear up to S = 2, but deviates significantly by S = 3. At S = 2 the temperature is calculated to be 1835 K, only 3% greater than that expected by linear extrapolation; increasing to S = 3, the modeled temperature reaches 2570 K, 12% greater than the linear response.

[34] Given the simple irradiance extrapolation described by equation (1), the total energy input to the atmosphere increases linearly between S = 0 and 3. The nonlinear increase in temperature demonstrated in Figure 3 thus indicates an attendant decrease in the effective cooling rate. Infrared radiation emitted by CO_2, NO, and O composes the majority of the total thermospheric cooling rate; the balance is made up by a combination of eddy and molecular conduction [*Roble et al.*, 1987; *Smithtro*, 2004]. At all values of S, cooling by CO_2 dominates the total, and is always more than an order of magnitude more important than loss from O. A decrease in the availability of CO_2 would thus reduce the effective cooling rate. This is, in fact, what occurs. At the top of the atmosphere, the CO_2 photolysis rate increases by more than 50% between S = 1 and S = 3. With no important thermospheric production terms to compensate [*Trinks and Fricke*, 1978], the CO_2 concentration decreases rapidly in the middle thermosphere [*Smithtro*, 2004].

[35] An analysis of the cooling contribution from NO is more complicated. Nitric oxide is formed via reactions between $N(^2D)$ and O_2 in the lower thermosphere and $N(^4S)$ and O_2 in the upper thermosphere, while the primary loss mechanism is the reaction $NO + N(^4S) \rightarrow N_2 + O$ [*Barth*, 1992]. The concentration of each of these reactants depends strongly on S, as well as the chemical reaction rates, which are strongly dependent on temperature. In turn, the relative importance of NO as a cooling mechanism varies nonlinearly. Over the course of the normal solar cycle, the net NO cooling rate increases by an order of magnitude, and goes from less than 2% of the total rate at S = 0 to 13% at S = 1. However, at higher values of S, enhanced loss processes stifle continued increases, and the contribution from NO begins to level off. The NO photolysis rate increases by 16% between S = 1 and S = 3, but more importantly the concentration of $N(^4S)$ increases by a factor of 4 over the same range. Ion-neutral chemical reactions produce the majority of atomic nitrogen [*Stolarski*, 1976], but photolysis of N_2 through predissociation in the wave-

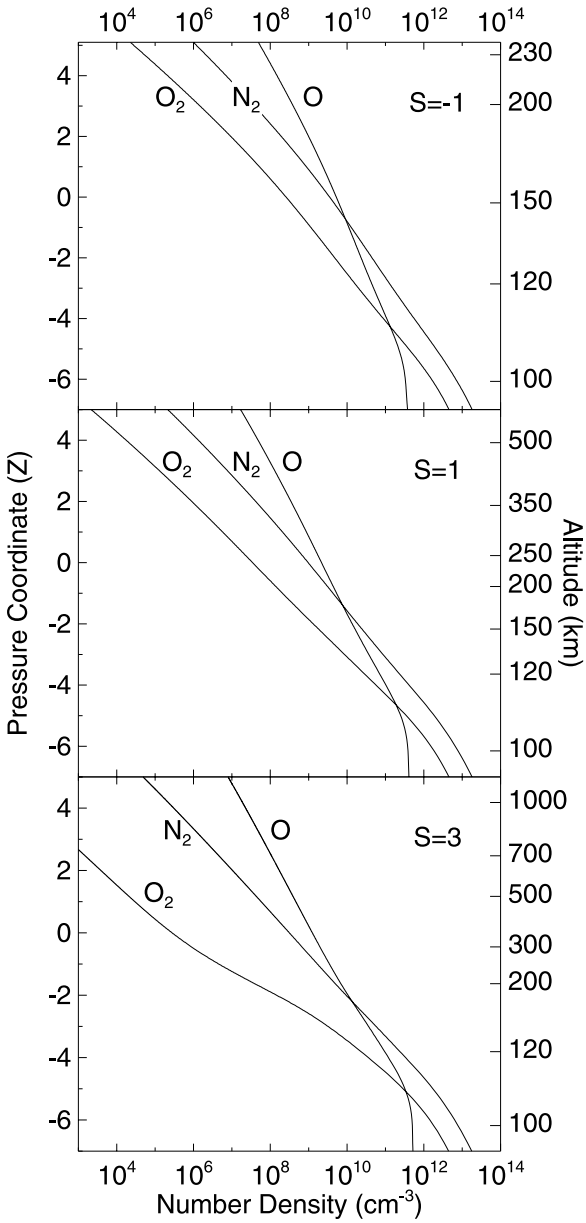

Figure 4. Global mean concentration of three major neutral species (N_2, O_2, and O), calculated using the GAIT model for increasing levels of solar activity: S = −1, S = 1, and S = 3. The profiles are plotted as a function of the pressure coordinate, Z, with the corresponding altitudes provided on the right-hand side.

length range 80–100 nm also contributes [*Richards et al.*, 1981]. The highly variable EUV wavelengths are responsible for both of these contributions, and thus the net N(^{4}S) production rate increases dramatically with S.

[36] While the overall concentration of atomic oxygen increases with S, radiational cooling due to O remains a minor contributor to the total rate. The net cooling is then determined primarily by the molecular species CO_2 and NO. Thus, because of enhanced molecular loss processes at higher values of S, the effective cooling rate decreases, resulting in the nonlinear temperature increase seen in Figure 3.

[37] Figure 4 shows global mean number densities calculated for three major neutral species, N_2, O_2, and O. The panels in Figure 4 correspond to increasing levels of solar activity. Figure 4 (middle) highlights normal solar maximum conditions (S = 1); Figures 4 (top) and 4 (bottom) correspond to S = −1 and S = 3, respectively. All of the profiles are plotted as a function of a pressure coordinate, defined as $Z = \mathrm{Log_e}[P_o/P]$, where P is the pressure, and P_o is a reference pressure of 50 μPa [*Roble et al.*, 1987]. A corresponding altitude scale is provided on the right-hand side of each panel.

[38] Plotting Figure 4 in pressure coordinates masks the changing scale heights, so as S increases, the most apparent effect is the depletion of the molecular gas, particularly O_2. Direct photolysis of O_2 contributes significantly to this depletion, and over the range of S = 1 to 3, the photolysis rate at the top of the atmosphere increases 35%, from 2.3×10^{-6} s^{-1} to 3.1×10^{-6} s^{-1}. Just as important is the increasing ionization rate. Through ion-neutral chemical reactions, nearly every ion produced results in the eventual dissociation of an O_2 molecule [*Stolarski*, 1976], and the net ionization rate at the top of the atmosphere increases 113% over the same range of S, from 4.6×10^{-7} s^{-1} to 9.8×10^{-7} s^{-1}. The increased dissociation of O_2 alters its profile, and by S = 3 the concentration drops significantly before recovering a diffusive equilibrium slope near Z = 0.

[39] In pressure coordinates, the overall shape of the O and N_2 profiles is relatively unchanged; note, however, that at a given pressure level the absolute concentration of these two species decreases with increasing S. This, of course, is due to the fact that at constant pressure the total gas concentration is inversely proportional to temperature. Since the neutral gas temperature increases with S, the concentrations of O and N_2 must decrease. At the model's lower boundary, the peak atomic oxygen concentration reflects the additional O_2 dissociation, increasing approximately 35% between S = −1 and S = 3.

5.2. Ionospheric Response

[40] In the thermosphere, the effects of extending S beyond the normal solar cycle were largely intuitive, characterized by changing temperatures and scale heights; more interesting results are found in the ionosphere. Figure 5 presents a comparison of the ion and electron density profiles calculated for three decreasing levels of solar activity, S = 0.0, −0.5, and −1.0, using the pressure coordinate Z as the vertical axis. Pressure is a convenient coordinate system for many reasons, but in the ionosphere it is particularly illuminating because the layers are effectively isobaric [*Rishbeth and Edwards*, 1989]. The NO^+ concentration shows a small discontinuity at Z = 3; this is an artifact of the approximate photoelectron solution described in paper 1 and has negligible impact on the overall solution.

[41] As the level of solar activity decreases, Figure 5 reveals that O^+, which composes the majority of the F_2 layer, is preferentially reduced versus the molecular ions making up the E and F_1 layers. By S = −1, the peak O^+ and NO^+ concentrations are nearly equal, producing a broad *F* region peak encompassing both the F_2 and F_1 layers. Figure 5 thus indicates a general climatological trend in which decreasing solar activity leads to decreasing importance of atomic O^+ in the F region.

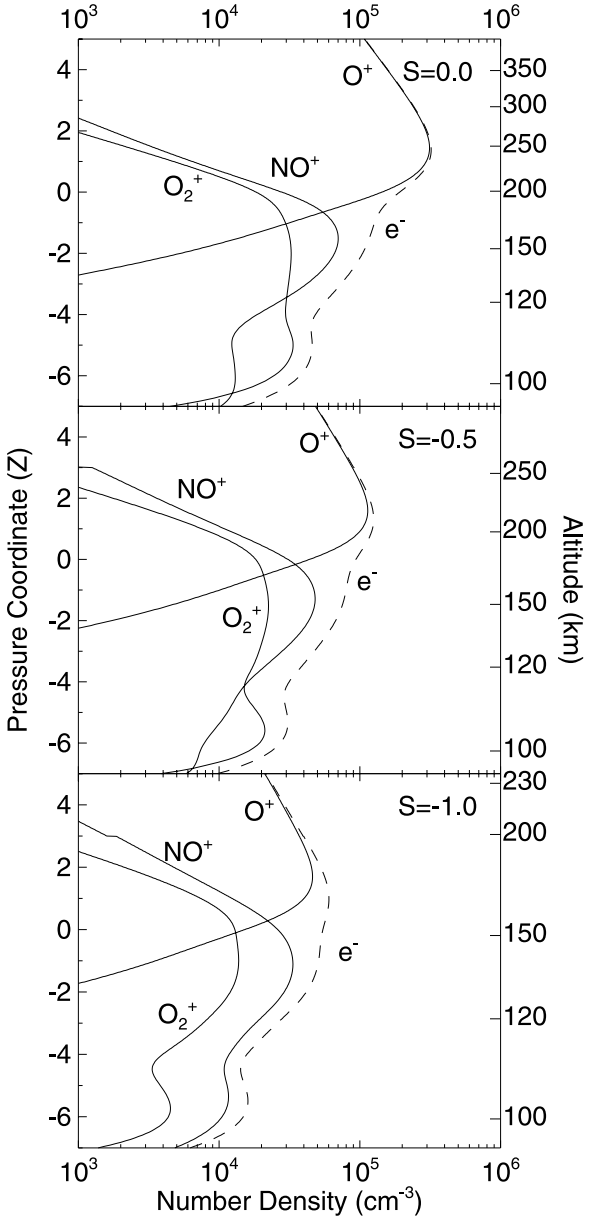

Figure 5. Global mean concentration of the ion and electron (dashed line) gases, calculated using the GAIT model for three decreasing levels of solar activity: S = 0, S = −0.5, and S = −1. The profiles are plotted as a function of the pressure coordinate, Z, with the corresponding altitudes provided on the right-hand side.

[42] The corresponding climatological response to extreme solar maximum conditions is represented in the three panels of Figure 6. Figure 6 again shows global mean number densities calculated for four ion species (O^+, NO^+, O_2^+, and N^+) as well as the electron gas, but this time the three panels correspond to increasing levels of solar activity. Figure 6 (top) highlights normal solar maximum conditions (S = 1); Figures 6 (middle) and 6 (bottom) correspond to S = 2 and S = 3 respectively. Again note that even as S increases and the atmosphere expands, the ionospheric layers are approximately isobaric.

[43] Overall, NO^+ exhibits relatively little change between S = 1 and S = 3. The peak density increases slightly, but the profile shape remains essentially stationary in pressure coordinates. The peak O_2^+ concentration also increases slightly, but only in the *E* region ionosphere. In the middle ionosphere, O_2^+ undergoes a steady decrease. This is due to the decreasing availability of neutral O_2, described previously. More interesting is the response of the two atomic ions, O^+ and N^+. As is evident from Figure 6, the N^+ concentration increases significantly over the range S = 1 to 3, while O^+ is relatively static.

[44] Figure 7 provides a complementary view of the ionospheric response over the entire range of solar activity, S = −1 to 3. Figure 7 (top) shows the peak concentrations of four ions (O^+, NO^+, O_2^+, and N^+), as well as the peak

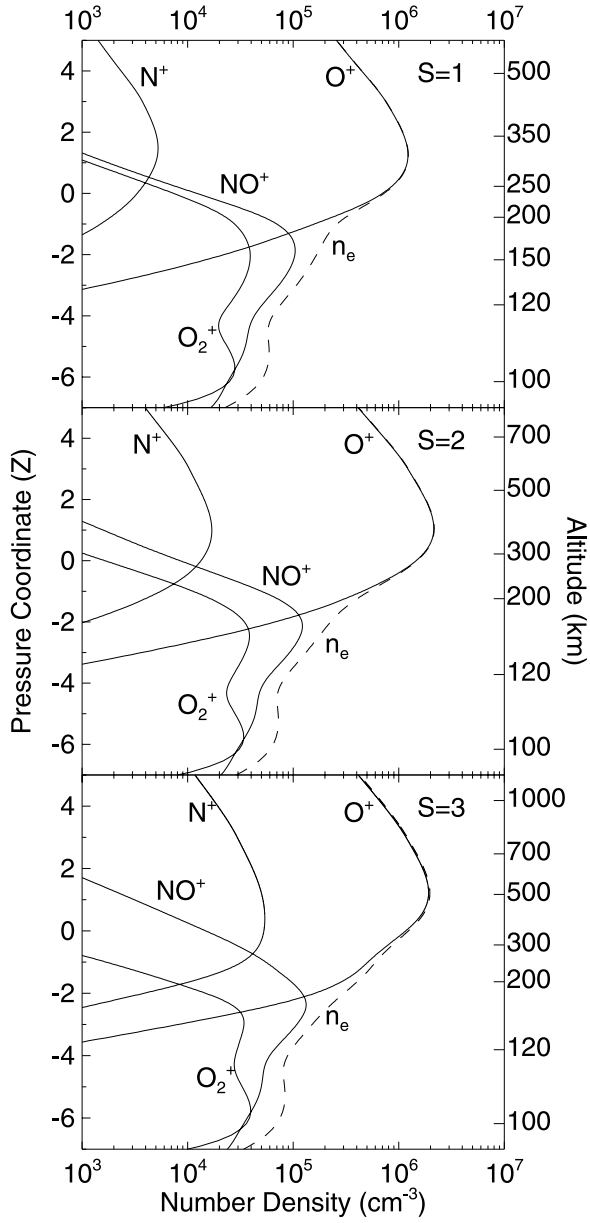

Figure 6. Global mean concentration of the ion and electron (dashed line) gases, calculated using the GAIT model for three increasing levels of solar activity: S = 1, S = 2, and S = 3. The profiles are plotted as a function of the pressure coordinate, Z, with the corresponding altitudes provided on the right-hand side.

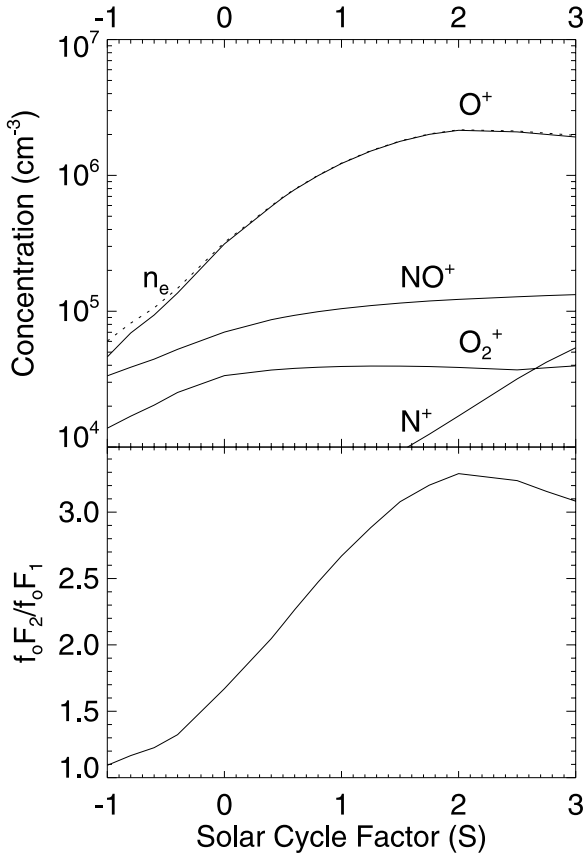

Figure 7. (top) Peak concentrations of four ions (O^+, NO^+, O_2^+, N^+) as a function of the solar cycle factor. A dotted line indicates the value of the peak electron density. (bottom) Ratio of the F_2 and F_1 critical frequencies (f_oF_2/f_oF_1), shown also as a function of S.

electron density, as a function of the solar cycle factor S. On the basis of these peak concentrations we see the molecular ion NO^+ increases monotonically over the full range of S. The peak concentration increases by a factor of 4 from 3.3×10^4 cm^{-3} at S = −1 to 1.3×10^5 cm^{-3} at S = 3. The behavior of O_2^+ is a little more complicated. Between S = −1 and 1 the peak concentration also increases monotonically, by a factor of 2.8, but it then decreases slightly at S = 2, before rising again at S = 3. From Figures 5 and 6, it is apparent the O_2^+ profile contains two peaks, one in the F_1 layer and one in the lower E layer. Over most of the range of S, the maximum concentration is found in the upper F_1 layer, but at higher S values there is less neutral O_2 available in the middle thermosphere and the O_2^+ concentration in the F_1 layer decreases. The dip observed in Figure 7 thus reflects a transition of the peak O_2^+ concentration from the F_1 layer to lower E layer.

[45] Figure 7 also provides a clear demonstration of the behavior of O^+ over the full range of S. As described previously in Figure 5, at low values of S, the concentration of O^+ decreases rapidly relative to the molecular ions. From S = 1 to −1, the peak O^+ concentration decreases by a factor of 26 from 1.2×10^6 cm^{-3} to 4.6×10^4 cm^{-3}; compare this to the molecular ions, which only decrease by a factor of 3 over the same range. At high S values the peak O^+ concentration not only plateaus, but reaches a local maximum near S = 2 and then decreases slightly toward S = 3.

[46] In contrast to the relatively stagnant behavior of the major ions, the peak N^+ concentration increases by more than an order of magnitude between S = 1 and 3, from 5.2×10^3 cm^{-3} to 5.4×10^4 cm^{-3}. As was noted previously, the concentration of neutral N(^{4}S) increases by a factor of 4 over the range S = 1 to 3, because of enhanced photolysis of N_2 as well as ionic chemical reactions. The additional atomic nitrogen is then readily ionized, resulting in the dramatic increase to N^+. Although highly speculative, model runs to values as high as S = 6 predict a continued increase in the N^+ concentration, until it represents a considerable fraction of the total ion density.

[47] Figure 7 (bottom) displays the ratio of the F_2 and F_1 critical frequencies (f_oF_2 and f_oF_1 respectively), again as a function of S. It is not always possible to identify a local F_1 layer maximum in the electron density profile, particularly beyond S = 1. For the purpose of this discussion, we calculate f_oF_1 on the basis of the electron density at the height where the sum of the molecular ions is a maximum. This approach identifies the correct value when a local maximum exists at the F_1 layer, and provides a representative number when it does not.

[48] The f_oF_2/f_oF_1 ratio provides a simple scalar indicator of many of the ionospheric features observed over the full range of solar activity. At low values of S, the ratio approaches a value of one, reflecting the rapid decline of O^+ versus the molecular ions. It is apparent that this transition reflects the extension of a trend that is ongoing even within the normal solar cycle; as S decreases from S = 1 to 0, this ratio decreases from 2.7 to 1.7. At higher levels of solar activity, the ratio responds to the O^+ plateau, exhibiting a peak value of 3.3 at S = 2, before declining slightly

[49] To this point, the model results have been plotted as a function of pressure, which masks expansion and contraction of the atmosphere. For an alternative perspective, Figure 8 depicts a contour plot of the electron density as a function of both altitude and solar activity. A dashed line in Figure 8 identifies the altitude of the peak electron density (h_mF_2). This height, which remained relatively fixed in pressure coordinates (Figures 5 and 6), climbs rapidly, reflecting the temperature increase described in Figure 3. Over the normal solar cycle range, the climatological h_mF_2 lies between roughly 250 km and 310 km. As S approaches S = −1, atmospheric contraction decreases h_mF_2 to 185 km. At the other extreme, h_mF_2 reaches 500 km at S = 3; at the same time, the width of the F layer is also expanding rapidly. The O^+ plateau described previously manifests itself as a local electron density maximum centered near S = 2.25, expanding upward in altitude.

[50] While the modeled N_mF_2 plateaus at extremely high solar activity, the same is not true for the total electron content (TEC). Simple physical arguments shed light on this difference. An estimate of TEC can be made by integrating the electron density profile from the height of peak up to infinity. The shape of the this profile is well approximated by an exponential decrease, governed by the plasma scale height. An integration thus results in the relationship TEC = $N_mF_2 \times H_p$, where H_p is the plasma scale height. Such an

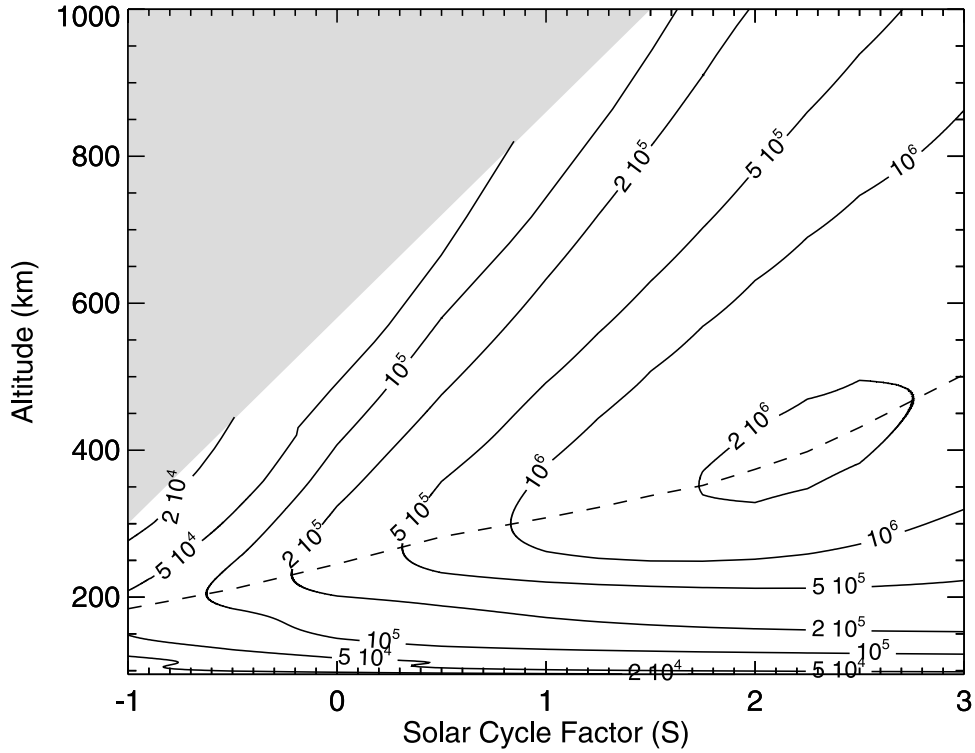

Figure 8. A contour plot of the global mean electron density (cm^{-3}), presented as a function of both solar cycle factor and altitude. The dashed line indicates the height of the peak electron density (h_mF_2). The normal solar cycle falls between S = 0 and 1.

approximation neglects the contribution of the bottomside F and *E* regions, and assumes H_p is constant, but provides a first-order estimate. Since H_p goes as the plasma temperature, so does TEC. This simple dependence merely reflects expansion and contraction of the isobaric F layer [*Rishbeth and Edwards*, 1989]. Over the course of a normal solar cycle, the modeled TEC increases from 7.4 to 37 TEC units, where 1 TEC unit = 10^{16} electrons/m^2. For S values larger than one, the nonlinear temperature increase outweighs the N_mF_2 plateau and TEC increases monotonically, reaching 95 TEC units at S = 2 and 135 units by S = 3.

5.3. O^+ Production and Loss

[51] We can better understand both the rapid decrease of the O^+ concentration at low S, and plateau feature at high S, by considering the production and loss terms at its peak (h_mF_2). Although an accurate solution for O^+ must include the effects of transport, over the range of S = −1 to 3 the peak concentration is approximated to within 25% by assuming photochemical equilibrium at that altitude. Figure 9 consists of three panels, all plotted as a function of the solar cycle factor, S. Figure 9 (top) gives the peak O^+ concentration, displayed previously in Figure 7. Figure 9 (middle) shows the production rate (cm^{-3} s^{-1}) at the peak; it is dominated by ionization, both photo and secondary, of O. Figure 9 (bottom) gives the loss rate (s^{-1}) at the O^+ peak. Two reactions, $N_2 + O^+$ and $O_2 + O^+$, dominate the total loss rate [*Schunk*, 1988].

[52] From Figure 9, it is immediately clear that as S decreases toward S = −1 the O^+ concentration suffers from both lower production and greater loss. The production curve is a convolution of the neutral O concentration and the incident photon flux; reductions in the EUV photon flux thus account for the trend observed in Figure 9 (middle). In fact, the lower flux must offset a slightly higher concentration of neutral oxygen available at the peak. Because the O_2 dissociation rate decreases with solar activity, the net concentration of O within the thermosphere is lower. However, the peak of the O^+ layer resides on a fixed pressure surface [*Rishbeth and Edwards*, 1989], thus the total gas concentration and neutral temperature on this surface are inversely related. As the neutral temperature decreases, the concentration of neutral O on a given pressure surface increases. Given that the net production rate is dominated by direct ionization of O, falling EUV fluxes drive the modeled behavior.

[53] Just as important to the final O^+ concentration is the rapidly increasing loss rate for S < 0. The principal loss mechanisms for O^+ involve chemical reactions with neutral N_2 and O_2. Again, because the O^+ peak resides on a fixed pressure surface, more N_2 and O_2 are available to react with O^+, increasing the loss rate. In addition, the rate coefficients for both of these reactions are roughly quadratic in temperature, increasing rapidly for low temperatures [*St.-Maurice and Torr*, 1978]. The molecular ions (NO^+ and O_2^+) on the other hand, are lost primarily through dissociative recombination with electrons. Since the electron density decreases with S, so does the effective loss rate for these ions, which partially offsets the lower production rates.

[54] Similar arguments can be made at the higher S values. From Figure 9 (middle), we immediately conclude that production is primarily responsible for the observed

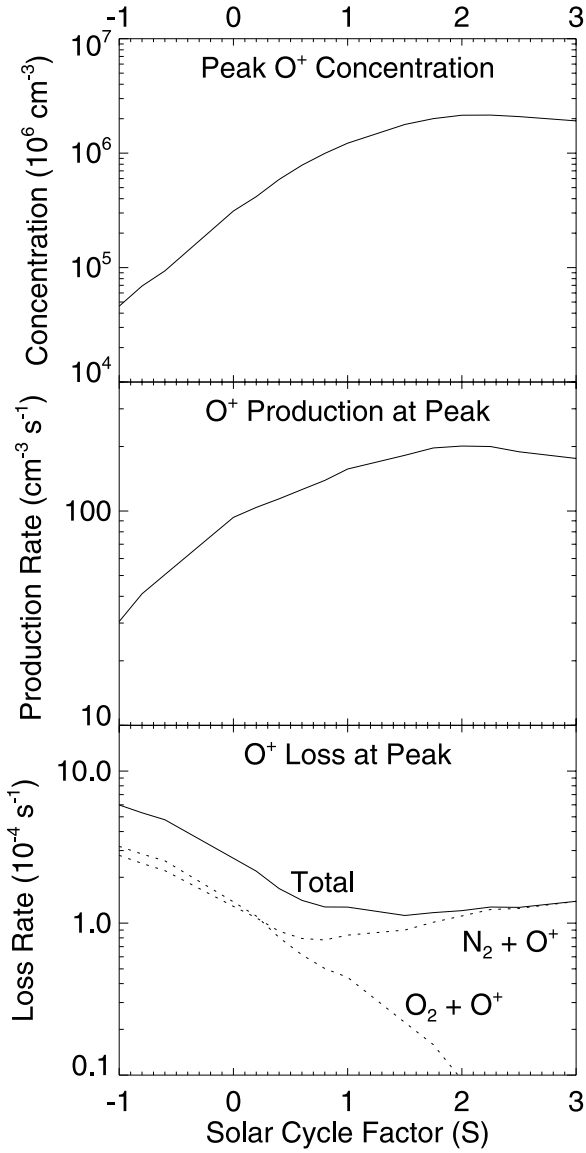

Figure 9. Shown are the (top) concentration, (middle) production rate, and (bottom) loss rate, at the O^+ peak, as a function of the solar cycle factor. Dotted lines delineate the contributions of two different chemical reactions to the total loss rate.

O^+ maximum near S = 2. On the basis of equation (1) the photon flux increases linearly with S. However, invoking yet again the idea of an isobaric O^+ layer, we expect a nonlinear decrease of the neutral O concentration at the peak due to the variation of the neutral gas temperature depicted in Figure 3. Additional dissociation of O_2 offsets this effect slightly by increasing the atomic oxygen mixing ratio, but at the O^+ peak the O concentration decreases by nearly a factor of 2 from S = 1 to 3. The convolution of linearly increasing photon flux and nonlinearly decreasing O concentration nearly balance beyond S = 2, giving the production curve seen in Figure 9.

[55] At low S values, reactions with N_2 and O_2 contribute roughly equally to the total O^+ loss rate. As S increases, the concentration of O_2 rapidly decreases (Figure 4), to point that its contribution becomes negligible. This leaves N_2 to control the total loss. Again, because of the inverse relationship between total concentration and temperature, there is less N_2 available at the peak as S increases. However, this decrease is offset by a roughly quadratic increase to the rate coefficient at high temperatures [*St.-Maurice and Torr*, 1978]. Combined, these opposing trends result in the curve shown in Figure 9 (bottom). Thus, between S = 2 and 3, competing factors in both production and loss of O^+ combine to produce a general plateau feature.

6. Discussion

6.1. Sensitivity to Boundary Conditions

[56] In model runs described above, the concentration of N_2 and O_2, as well as the neutral gas temperature, were held fixed at the lower boundary. As described in paper 1, these boundary conditions are based on global averages calculated using the empirical MSIS model. We specifically chose the lower boundary altitude (95 km) to coincide with the global average mesopause because at this altitude the MSIS global averages are constant to within a few percent over the course of the normal solar cycle.

[57] While varying the solar activity level from S = −1 to 3, we continued to assume these parameters were fixed. We rationalized this assumption using the results of Table 1, which showed that even as the EUV energy flux changes by a factor of 25, very little additional energy penetrates to the mesosphere. To investigate fully the sensitivity of the mesopause over the full range of S would require expanding the model's boundary to lower altitudes, but on the basis of the normal solar cycle variation of MSIS we estimated it should be less than 10%. A reasonable question is whether the model results presented above are affected by changing the boundary conditions on the order of 10%.

[58] To test the model's sensitivity to the lower boundary conditions, we increased the neutral gas concentration and temperature by 30% and recomputed the results over the same range of S = −1 to 3. This process was repeated after decreasing the boundary conditions by 30%. Given the extent of the changes made to the boundary conditions, the resulting effects were relatively small. Across the full range of ±30%, the resulting neutral gas exospheric temperature varied only 3–15%. Peak concentrations of the various ions were similarly affected. N_mF_2 varied by 16–33% over the full range and N_mF_1 by 1–12%; however, the overall morphology described previously did not change.

[59] In Figure 10 we show the f_oF_2/f_oF_1 ratio as a function of the solar cycle factor S. The solid line corresponds to the original results shown in Figure 7, while the dotted (dashed) line reflects a 30% increase (decrease) to the lower boundary conditions. The shape of all three curves is largely the same. As S approaches S = −1, the three ratios tend toward unity, with only 4% variance imparted by altering the lower boundary conditions ±30%. At higher values of S, the difference across the three solutions increases to 20%, but again the shape of the curve remains the same.

[60] The concentration of CO_2 constitutes another important lower boundary condition. The GAIT model currently uses a mixing ratio of 360 ppm based on a fit to experimental data provided by *Fomichev et al.* [1998]. In addition to the general uncertainty surrounding the current value,

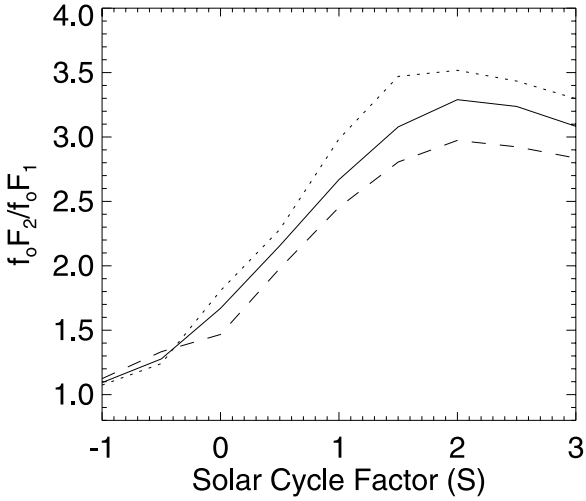

Figure 10. Modeled f_oF_2/f_oF_1 ratio is shown as a function of the solar cycle factor, using three different lower boundary conditions. The solid line corresponds to the standard results, the dotted line represents a 30% increase to the lower boundary conditions, and the dashed line represents a 30% decrease.

there is also significant interest in understanding the ionospheric impacts of a predicted doubling in such "greenhouse" gases over the next century. *Roble and Dickinson* [1989] first examined the thermospheric response to increased CO_2, and predicted significant additional cooling. Since that time there has been further theoretical [*Rishbeth*, 1990] and experimental work in an effort to find evidence supporting global secular change in the thermosphere [*Emmert et al.*, 2004] and ionosphere [*Upadhyay and Mahajan*, 1998; *Danilov*, 2001].

[61] To investigate the sensitivity of the GAIT results to such changes, we reran the model after both increasing and decreasing the CO_2 mixing ratio by 25%. Similar to the results of *Roble and Dickinson* [1989], increasing the CO_2 mixing ratio to 450 ppm lowered the exospheric temperatures; the temperature dropped 20 K at solar minimum, but only 10 K at solar maximum. Similarly, lowering the mixing ratio to 270 ppm increased the exospheric temperatures. Over the full range of S, the largest relative temperature change occurred at S = −1; a mixing ratio of 450 ppm lowered the temperature 13 K (3%), while 270 ppm raised it 17 K (4%). These relatively small temperature changes had very small absolute effects on the ionosphere, and no effect on the climatological behavior described earlier. In terms of the scalar f_oF_2/f_oF_1 ratio, plots created using the three different boundary conditions appeared essentially identical. Maximum differences between the solutions were on the order of 2%. On the basis of these results, and those above, we conclude the lower boundary conditions do not strongly affect the morphology described in section 5.

6.2. Sensitivity to EUV Representation

[62] As described previously, the climatological variation of the ratio f_oF_2/f_oF_1 results from changes to both the thermosphere, through the neutral gas temperature, as well as the flux of ionizing photons. It would therefore be reasonable to ask how sensitive the results are to a specific model of the input solar irradiance, i.e., the wavelength distribution of the EUV photons.

[63] In paper 1, we compared the integrated EUV energy flux predicted by four different irradiance models over the course of the typical solar cycle. In addition to the VUV model [*Woods and Rottman*, 2002], this included the empirical Solar2000 (S2000) [*Tobiska et al.*, 2000] and EUVAC [*Richards et al.*, 1994] models, as well as the semiphysical NRLEUV model [*Warren et al.*, 2001] introduced earlier. Our work showed that the integrated energy flux predicted by the models differed significantly, in both absolute scale and dynamic range. A similar study by *Lean et al.* [2003], involving three of the models, reached similar conclusions. In addition to the energy flux, *Lean et al.* [2003] also considered the spectral response of the models, and again found significant differences. A comparison of these four irradiance models thus amounts to a test of the integrated wavelength sensitivity.

[64] Each of these four irradiance representations were used in conjunction with the GAIT model to generate output for solar activity levels ranging from S = −1 to 3. For intercomparison, we again rely on the f_oF_2/f_oF_1 ratio as a scalar representation of overall state of the ionosphere. Figure 11 presents the f_oF_2/f_oF_1 ratios calculated using each of the four irradiance models, as well as an artificial spectrum described below. Figure 11 (top) gives the ratio as a function of the solar cycle factor S, while Figure 11 (bottom) normalizes the output to the calculated exospheric temperature. In Figure 11, the solid line represents the ratio calculated with the VUV model and is identical to the results presented earlier in Figure 7.

[65] The EUVAC model produces results very similar to the VUV; the correlation improves slightly when plotted as a function of temperature. The ratios calculated with the S2000 model are generally smaller than the VUV results, but follows the same trend. The correlation is again improved when the ratio is plotted as a function of temperature. Overall, the S2000 ratios are smaller than those computed with the VUV or EUVAC models. This difference exists because S2000 generally produces lower N_mF_2 values for the same solar activity level. Because of the smaller dynamic range of the NRLEUV model the neutral gas temperature undergoes much less variation over the range S = −1 to 3 (see paper 1). As a result, the ratios computed with NRLEUV do not exhibit the expected morphology when plotted as a function of S. However, when recast using the exospheric temperature, we find the NRLEUV results are indeed very similar to the other models. The NRLEUV results simply span a subset of the full morphology, corresponding to a smaller temperature range. Again, given the differences described in paper 1 and by *Lean et al.* [2003], this is not surprising.

[66] By normalizing the ratio to the exospheric temperature, which reflects the overall state of the thermosphere, all four irradiance models come into reasonable agreement, and certainly exhibit the same general trends. This reemphasizes that the morphology of the f_oF_2/f_oF_1 ratio depends fundamentally on the underlying thermosphere, rather than any specific representation of the EUV irradiance. A final check of the wavelength sensitivity is made using a completely artificial input spectrum.

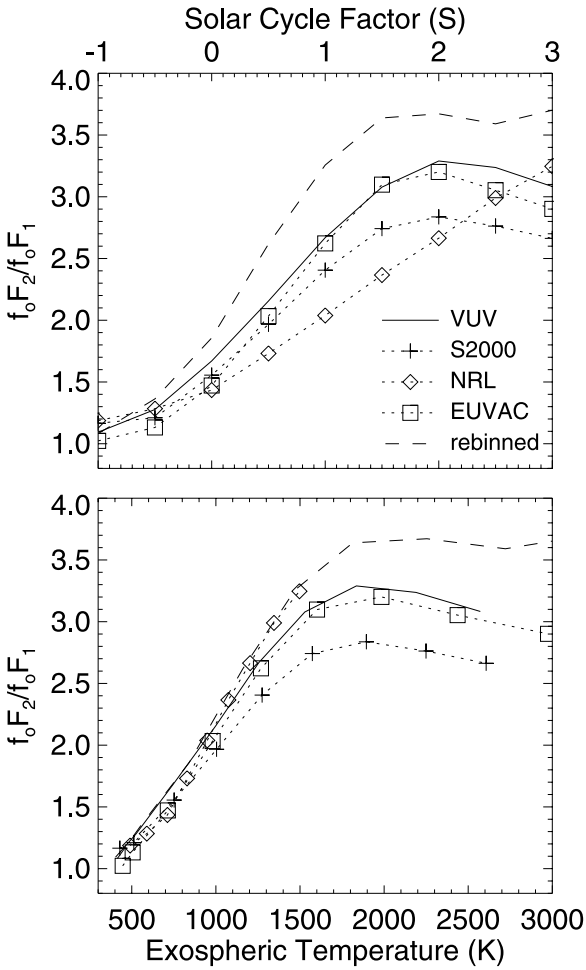

Figure 11. Comparison of the f_oF_2/f_oF_1 ratio calculated using four different solar irradiance models as well as an artificial photon redistribution. The ratio is (top) plotted as a function of the solar cycle factor and (bottom) normalized to the neutral gas exospheric temperature. The solid line corresponds to the standard irradiance input, the VUV model [*Woods and Rottman*, 2002], while the dotted lines with crosses, diamonds, and squares correspond to the Solar 2000 version 2.21 [*Tobiska et al.*, 2000], NRLEUV [*Warren et al.*, 2001], and EUVAC [*Richards et al.*, 1994] models, respectively. The dashed line identifies results obtained using an artificially rescaled spectrum described in the text.

[67] For very low solar activity levels, the extrapolation described by equation (1) produces zero flux in some of the highly variable wavelength bins dominated by coronal emissions. Earlier we recognized that even with no coronal emission, less variable, underlying chromospheric emission should still remain. We might therefore question whether zeroing the flux at specific wavelengths strongly influences the result as S approaches S = −1. To test this sensitivity we redistributed the input photons, creating an artificial input spectrum. For a given value of S, the model first calculated the spectrum using equation (1) and the VUV irradiance model. From this spectrum, the model calculated the total input EUV energy flux and then redistributed this energy equally between all of the EUV bins according to the average wavelength within the bin. The result is a completely artificial spectrum in which all of the wavelength bins are guaranteed to have nonzero flux.

[68] The f_oF_2/f_oF_1 ratios computed using the redistributed spectra are plotted using a dashed line in Figure 11. As might be expected, the model results differ fairly significantly when using the artificial spectrum. In general, temperatures computed with the rebinned spectra are significantly higher than the other EUV models; for example, at solar minimum, S = 0, the standard models converge near 730 K, while the artificial spectrum gives 840 K. Higher temperatures for a given value of S shift the f_oF_2/f_oF_1 curve to the left. As with NRLEUV model, normalizing the curve to the computed thermospheric temperature removes most of the differences, although the absolute value of the ratio remains larger. This is not surprising; by redistributing the EUV photons we have altered the species-dependent ionizations rates.

[69] At low solar activity levels, the ratio computed with the rebinned spectra agree fairly well with the other models, particularly when the results are normalized to the exospheric temperature. In section 5.3 we described how the modeled behavior of O^+ required both decreasing temperatures and less photoionization. Given that the artificial spectrum produces essentially the same result as the other models, we can conclude it is not driven by specific wavelength bands being set to zero, and is instead a feature of overall decreasing ionization rates.

6.3. Ionospheric G Conditions

[70] Ground-based soundings of the ionosphere routinely record the critical frequencies of the various ionospheric layers. In cases where the N_mF_2 is less than N_mF_1, the F_2 peak is not observable from the ground, and a descriptive qualifier "G" is added to the measurement on the basis of guidelines outlined in the *URSI Handbook of Ionogram Interpretation and Reduction* [*Piggott and Rawer*, 1978]. The qualifier G specifies that a measurement of the F_2 peak was not possible because the electron density was too low to be measured. Such "G conditions" have long been associated with the negative phase of ionospheric storms [*Norton*, 1969], when energy deposition associated with enhanced geomagnetic activity alters the neutral atmospheric composition, but they are also fairly common in the quiet ionosphere at solar minimum during the summer [*Pavlov and Buonsanto*, 1998]. While the 1-D GAIT model cannot provide insight into the dynamical changes resulting from geomagnetic activity, it is applicable to the quiet solar minimum ionosphere.

[71] *Lobzin and Pavlov* [2002] conducted a statistical study of the occurrence of G conditions covering the period 1957–1990. As expected, they found a strong correlation between the occurrence probability and the 3-hour geomagnetic Kp index, and related this to storm-time depression of N_mF_2. The dependence of G conditions on the F10.7 solar proxy was more complicated. The G condition occurrence probability was high for both low and high solar activity, and reached a minimum at middle levels (F10.7 between 144 and 170) [*Lobzin and Pavlov*, 2002]. Strong geomagnetic storms are more frequent during high solar activity, and the authors suggested the increased occurrence of G

conditions at high F10.7 was due to a positive correlation between Kp and F10.7.

[72] For low solar activity levels, *Lobzin and Pavlov* [2002] showed that the occurrence of G conditions depends more on an initially strong F_1 layer, rather than dynamic depression of N_mF_2 during a storm. If the ratio f_oF_2/f_oF_1 is initially close to one, relatively small perturbations such as a poleward neutral wind can induce G conditions in the midlatitude ionosphere. In other words, their results show that the ionosphere is predisposed to G conditions at solar minimum. This is exactly the climatological result implied by the GAIT model. On the basis of the GAIT model result, we expect G conditions would become a regular feature of the daytime ionosphere as solar activity approaches levels representative of the Maunder Minimum epoch.

[73] It is interesting to note that *Ratcliffe* [1972] predicted some of the same aspects of this climatological behavior using a simplified analytic analysis. Focusing solely on the F_1 layer and assuming photochemical equilibrium for NO^+, *Ratcliffe* [1972] determined that a well-defined F_1 peak depended on the altitude of maximum photoionization relative to a so-called ''transition height''. The transition height was defined as the altitude where production of NO^+ via the reaction of $O^+ + N_2$ is balanced by loss through dissociative recombination. *Ratcliffe* [1972] showed that a local F_1 layer maximum is visible only when the photoionization peak is below this transition height. The difference between these two heights determines the relative magnitude of the F_1 peak. When the altitude of maximum photoionization occurs above the transition height, the F_1 peak becomes hidden within the larger *F* region electron density.

[74] Expanding on this analysis, *Ratcliffe* [1972] further argued that the transition height moves to higher altitudes as the total electron density decreases, hence the F_1 peak is more pronounced at solar minimum than maximum. In addition, we know that the altitude of maximum photoionization decreases with the neutral gas temperature, and thus solar activity. This effect further increases the separation between the two heights, enhancing the F_1 peak. The *Ratcliffe* [1972] analysis disregards the relative magnitude of the F_2 layer, but can be used to explain some of the results seen in Figures 5 and 6, and complements the approach taken in section 5.3, by focusing on the F_1 rather than F_2 layer.

6.4. F Region Saturation at Solar Maximum

[75] Previous work by a number of authors has demonstrated that in general, ionospheric parameters, such as the F region critical frequency (f_oF_2) and TEC, increase with solar activity; however, the correlation between these observables and the F10.7 solar proxy is complicated [*Balan et al.*, 1994a; *Richards*, 2001; *Sethi et al.*, 2002; *Liu et al.*, 2003, 2004]. For example, when *Liu et al.* [2004] examined the behavior of the monthly median f_oF_2 over Wuhan, China (114.4°E, 30.6°N; 45.2° dip), they found the average local noon values appeared to saturate when F10.7 exceeded roughly 200. *Balan et al.* [1994a] reported a similar saturation effect in their study of the electron content measured over several stations; they suggested that the electron content responds linearly to the solar EUV input, and that the observed behavior merely reflects a breakdown of the desired linear relationship between F10.7 and the actual EUV irradiance [*Balan et al.*, 1994a, 1994b].

[76] In the absence of regular EUV irradiance measurements, widespread use of F10.7 as a proxy has led to the current situation, in which it is difficult to separate the observed behavior of the ionosphere from uncertainties associated with the solar proxy. With a modeling approach, we are not so constrained, since we can force a purely linear increase to the solar EUV flux. In Figure 12, we examine the behavior of ionospheric parameters typically cited in the literature, over a range of S = 0 to 2. A second *x* axis gives the corresponding value of the P index introduced in section 3. Over the range of S displayed in Figure 12, the P index increases from 70 to 390, where P = 70 and P = 230 are assumed to represent typical solar minimum and maximum conditions, respectively. In recent history, the daily P index has rarely exceeded a value of 300, the latest periods being January and February 1991 when P reach a maximum of 337. The results in Figure 12 thus represent an extrapolation to irradiance levels just beyond the range of ''normal'' solar behavior.

[77] Four panels in Figure 12 delineate various ionospheric parameters as calculated by the GAIT model. Figure 12a gives N_mF_2, which was presented previously in Figure 7, but the range of S is now reduced. Figures 12b, 12c, and 12d give f_oF_2, TEC, and an effective F layer slab thickness, respectively. The effective slab thickness is found by simply dividing TEC by N_mF_2. According to the arguments of section 5.2, this thickness is then roughly proportional to the plasma scale height, H_p, and therefore the plasma temperature.

[78] Given the underlying relationships between N_mF_2, f_oF_2, and TEC, if one of these parameters were to respond linearly to the solar irradiance, the other two could not. Over the course of the typical solar cycle (S = 0 to 1), it is apparent from Figure 12 that f_oF_2 exhibits the most linear increase. Even so, for higher levels of activity, the f_oF_2 curve begins to plateau. We have already shown how concomitant changes in the underlying thermosphere create a plateau in N_mF_2 near S = 2. It is therefore not surprising that f_oF_2, which goes as the square root of N_mF_2, would also plateau, beginning at even lower values of S. Supporting this result are the observations of the monthly median f_oF_2 reported by *Liu et al.* [2004], which show the same general behavior as our GAIT model results. It is important to reiterate that the N_mF_2 and f_oF_2 plateaus demonstrated here are predicted to form even as the solar irradiance continues to increase linearly.

[79] Unlike N_mF_2 and f_oF_2, the GAIT model results indicate TEC should continue to increase rapidly over the entire range of S. This increase is driven primarily by the expanding F region, as depicted in Figure 12d. This behavior runs counter to that observed by *Balan et al.* [1994a], who reported saturation of the electron content over several stations when F10.7 exceeded roughly 200. It is unclear how much their results would differ if recast in terms of the more linear P index, but if the saturation remains, the most likely cause is continued nonlinearity of the solar proxy. Our results therefore lend credence the conclusions of *Balan et al.* [1994a, 1994b].

6.5. Helium Budget

[80] Our GAIT model results also have applicability to the problem of the Earth's helium budget. Early work by a

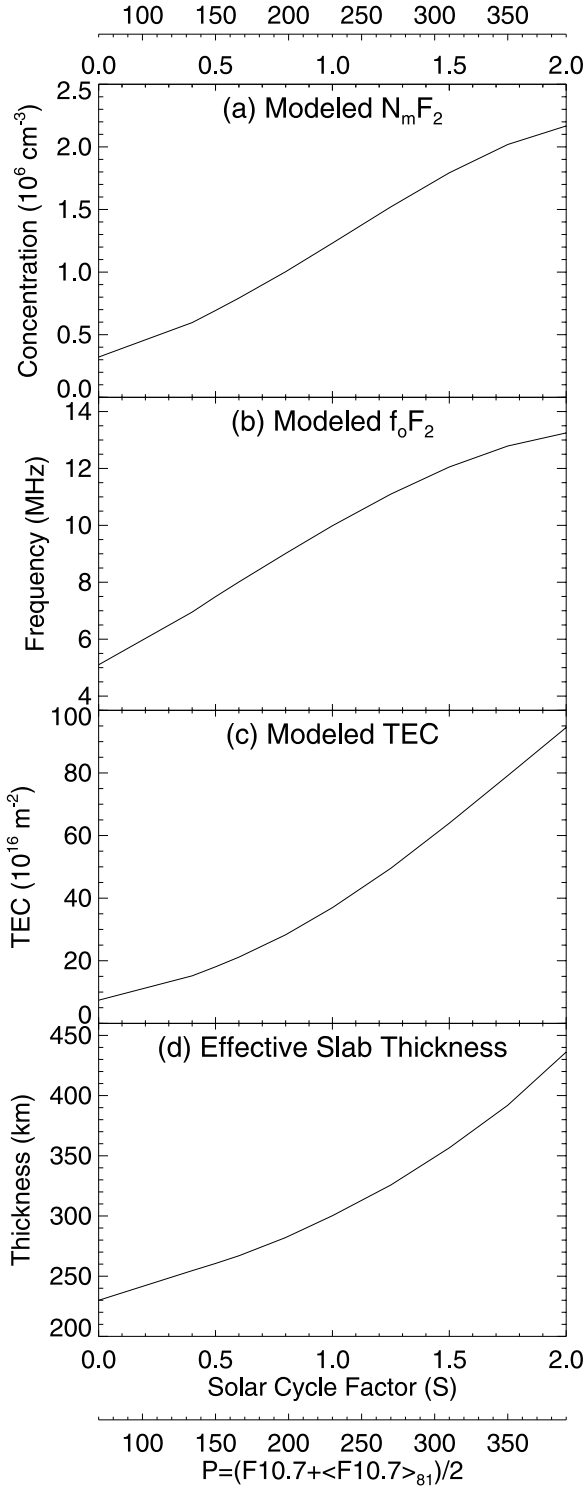

Figure 12. Shown are the GAIT modeled (a) N_mF_2, (b) f_oF_2, (c) TEC, and (d) effective F layer slab thickness. The plots are given as a function of the solar cycle factor, ranging from S = 0 to 2, as well as the P index, where P = (F10.7 + $\langle$F10.7$\rangle_{81}$)/2 [*Richards et al.*, 1994].

number of authors [*Nicolet*, 1957; *Bates and McDowell*, 1957; *MacDonald*, 1963] identified difficulties in explaining the concentration of helium in the atmosphere, a problem that persists to this day. In the case of helium, the standard Jeans mechanism of thermal escape is not sufficient to balance the known production rate via radioactive decay in the Earth's crust. In fact, given the difference in production and loss rates, the present concentration of helium would accumulate in just a few million years, far shorter than the age of the Earth. Additional, nonthermal loss mechanisms have been advanced to bridge this divide [*Axford*, 1968; *Michel*, 1971; *Sheldon and Kern*, 1972], but they remain speculative. *Hunten* [1973] proposed a less exotic theory; he noted that only intermittent periods of enhanced exospheric temperatures (2000 K) are needed to supplement the average loss rate, and calculated that the "hot episodes would have to last about 2% of the total time. Since the time constant for filling the atmosphere is around 10^6 years, these periods could be extremely infrequent" [*Hunten*, 1973].

[81] According to the GAIT model results (Figure 3), the 2000 K temperatures needed for the Hunten theory arise for activity levels near S = 2.2. These are of course global average results, and locally these temperatures would be reached for even lower values of S. Resolution of the helium problem using traditional Jeans escape thus points to extreme solar maximum conditions as a recurring solar feature.

7. Conclusion

[82] This work examined the response of the ionosphere and thermosphere to hypothetical extremes in the input solar irradiance. Extremely low solar flux levels were motivated by the Maunder Minimum epoch. Previous studies of cosmogenic isotopes [*Eddy*, 1976; *Webber and Higbie*, 2003] and Sun-like stars [*Baliunas and Jastrow*, 1990; *White et al.*, 1992; *Radick et al.*, 1998; *Radick*, 2003] were used to justify our assertion that the solar irradiance during Maunder Minimum was indeed dramatically different than modern solar minimum. The case for extremely high solar activity was motivated by the Grand Maximum epoch (1100–1250 A.D.) [*Eddy*, 1976], as well as the Sun's location within the emission distribution of Sun-like stars [*Radick et al.*, 1998; *Radick*, 2003].

[83] To facilitate an extrapolation of the input solar irradiance, we introduced a solar cycle factor, S, for which S = 0 corresponds to normal solar minimum and S = 1 to solar maximum. The input solar irradiance was then formed by linearly extrapolating each wavelength bin using equation (1). The solar cycle factor is related to the more familiar 10.7 cm radio flux through the P index, introduced by *Richards et al.* [1994]. We chose to use S, rather than a physical proxy, in order to separate our results from questions regarding the linearity of these proxies at high solar activity levels [*Balan et al.*, 1994a, 1994b; *Richards et al.*, 1994].

[84] Output from the GAIT model was examined over a range of S = −1 to 3. On the basis of the arguments of *Lean et al.* [2001] and J. L. Lean (private communication, 2004), Maunder Minimum irradiance levels were assumed to fall between S = −0.5 and S = −1.0. Our motivation provided little quantitative guidance for an upper bounds on S, so we arbitrarily used S = 3. On the basis of the recent work of *Solanki et al.* [2004] this represents greater solar activity than exhibited by the Sun in the past few thousand years,

but for the purposes of this modeling effort, extending to S = 3 allows us to capture a distinct morphology within the ionosphere.

[85] Within the thermosphere, neutral gas temperatures responded linearly to the input EUV energy flux over the range S = −1 to 1. Beyond S = 1, the modeled exospheric temperature began to increase nonlinearly, even as the input energy increased linearly. We argued this deviation was caused by a simultaneous decrease in the molecular gases most important to radiative cooling, primarily CO_2. In addition to expansion, the general response of the neutral gas to increasing solar activity levels involved a reduction of molecular species, through enhanced dissociation, resulting in increased relative concentrations of atomic oxygen and nitrogen.

[86] At both high and low solar activity levels, the behavior of the thermosphere drove the ionospheric response. Continuing a trend observed within the normal solar cycle, the concentration of O^+ declined rapidly relative to the molecular ions, as S dropped to levels representative of Maunder Minimum. We quantified this using the ratio of the critical frequencies, f_oF_2/f_oF_1, and showed it goes to unity as S approaches S = −1. Considering photochemical equilibrium at the O^+ peak, we argued the effect stemmed from both a lower photoionization rate, and just as importantly, a higher loss rate. Given the isobaric nature of the F region [*Rishbeth and Edwards*, 1989], the loss rate increases primarily because lower temperatures imply higher concentrations of the reactants, N_2 and O_2.

[87] At the other extreme, increasing solar activity beyond S = 1 initially drove the f_oF_2/f_oF_1 ratio higher, to a maximum of 3.3 at S = 2. However, beyond this value the ratio leveled off and then declined slightly, reflecting a broad N_mF_2 plateau. Again, photochemical equilibrium was used to understand this behavior. We argued that competing processes in both the production and loss were responsible. On the production side, higher photon fluxes were eventually offset by less atomic oxygen available for ionization because of atmospheric expansion. Less N_2 and O_2 were also available for chemical loss, but this was offset by increasing chemical reaction rate coefficients. On the whole, both production and loss rates leveled off beyond S = 2, producing a broad N_mF_2 plateau.

[88] Although the model results are arguably more speculative the farther one moves from the normal solar cycle, important applications exist in the vicinity of both solar minimum and maximum. The results obtained at low solar flux levels can be used to explain the preponderance of ionospheric G conditions observed near solar minimum. G conditions, when N_mF_2 is less than N_mF_1, are typically associated with the negative phase of ionospheric storms. However, a statistical study by *Lobzin and Pavlov* [2002] found an increasing likelihood of occurrence as F10.7 decreases. On the basis of the GAIT model results we conclude that as the solar EUV irradiance decreases, the f_oF_2/f_oF_1 ratio approaches unity, and the ionosphere is predisposed to G conditions.

[89] As described in section 6.4, f_oF_2 is predicted to increase nearly linearly over the course of the normal solar cycle, but soon after begin to plateau. This effect has been observed by *Liu et al.* [2003, 2004] at a number of different locations. *Liu et al.* [2003] cited the work of *Balan et al.* [1994a, 1994b] and suggested the plateau effect was caused, at least in part, by a nonlinear relationship between the solar EUV irradiance and the F10.7 proxy. Independent work [*Richards et al.*, 1994] supports this idea, but our results indicate that it is not the only causal factor. Instead, the effect reported by *Liu et al.* [2003, 2004] is likely caused by a combination of both the inherent plateau described here and EUV saturation with respect to F10.7.

[90] The model results also have applicability to the problem of the Earth's helium budget. Assuming that helium loss is controlled by traditional Jean's thermal escape, the current concentration of atmospheric helium requires periodic increases of the neutral gas exospheric temperature beyond 2000 K [*Hunten*, 1973]. According to Figure 3, global average temperatures will reach these levels at roughly S = 2.2 (P = 420). In contrast to the work of *Solanki et al.* [2004], this suggests extreme solar maximum conditions could be a recurring feature.

[91] While varying the solar irradiance outside of the normal solar cycle, we must be cognizant of the many assumptions inherent to the model and the possibility that they may break down. One of the biggest assumptions is that the lower atmosphere remains unaffected throughout the range S = −1 to 3. We examined this issue as it related to the direct transfer of energy and found relatively little change in the amount of energy that penetrates to the mesosphere. Overall, the model results were also found to be relatively insensitive to changes in the lower boundary conditions.

[92] The wide temperature range covered in Figure 3 could impact the model results. Over such a range, we have to question many of the chemical reaction rate coefficients. Most of these coefficients have been fit over a narrow temperature window, if at all. As the temperatures exceed 2500 K, we must also begin to consider the high-energy tail of the particle distribution. New reactions, which were previously not important, might have a major impact for particles with a few eV of thermal energy. Another concern is the escape of this tail population into the plasmasphere. We have yet to investigate the importance of an O^+ escape flux as the temperatures increase.

[93] Additional work is planned to address the ionosphere's diurnal behavior outside the normal solar cycle. Molecular ions recombine quickly in the nighttime ionosphere, while O^+ is maintained by downward transport. Therefore the f_oF_2/f_oF_1 ratio used throughout this paper obviously undergoes a strong diurnal variation. Future work will examine this using the Time-Dependent Ionospheric Model (TDIM) [*Schunk*, 1988]. The three-dimensional TDIM uses a Lagrangian approach, following individual magnetic flux tubes as they rotate in time. Currently the TDIM employs the empirical MSIS model to specify the underlying thermosphere, but we can substitute this with a parameterization based on the work from this paper. By using the GAIT model results to specify the thermosphere, and reducing the input solar irradiance, we will be able to explore the diurnal variation of the ionosphere outside the normal solar cycle.

[94] **Acknowledgments.** This research was supported by NASA grant NAG5-8227 and NSF grant ATM-0000171 to Utah State University. Christopher Smithtro was supported by the Air Force Institute of Technol-

ogy. The authors would like to thank Judith Lean and Harry Warren for their help in specifying the Maunder minimum irradiance. Vince Eccles recognized a connection between the model results and the global helium budget. Solar2000 irradiances are provided courtesy of W. Kent Tobiska and SpaceWx.com. The EUV irradiance models have been developed with funding from NASA and ONR. The views expressed in this article are those of the authors and do not necessarily reflect the official policy or position of the U.S. Air Force, the Department of Defense, or the U.S. Government.

[95] Arthur Richmond thanks Pierre-Louis Blelly and Dirk Lummerzheim for their assistance in evaluating this manuscript.

References

Axford, W. I. (1968), The polar wind and the terrestrial helium budget, *J. Geophys. Res.*, *73*(21), 6855–6859.

Balan, N., G. J. Bailey, B. Jenkins, P. B. Rao, and R. J. Moffett (1994a), Variations of ionospheric ionization and related solar fluxes during an intense solar cycle, *J. Geophys. Res.*, *99*(A2), 2243–2253.

Balan, N., G. J. Bailey, and R. J. Moffett (1994b), Modeling studies of ionospheric variations during an intense solar cycle, *J. Geophys. Res.*, *99*(A9), 17,467–17,475.

Baliunas, S. L., and R. Jastrow (1990), Evidence for long-term brightness changes of solar-type stars, *Nature*, *348*, 520–523.

Barth, C. A. (1992), Nitric oxide in the lower thermosphere, *Planet. Space Sci.*, *40*, 315–336.

Bates, D. R., and M. R. C. McDowell (1957), Atmospheric helium, *J. Atmos. Terr. Phys.*, *11*, 200–208.

Danilov, A. D. (2001), Do ionospheric trends indicate to the greenhouse effect?, *Adv. Space Res.*, *28*(7), 987–996.

Eddy, J. A. (1976), The Maunder minimum, *Science*, *192*, 1189–1202.

Emmert, J. T., J. M. Picone, J. L. Lean, and S. H. Knowles (2004), Global change in the thermosphere: Compelling evidence of a secular decrease in density, *J. Geophys. Res.*, *109*, A02301, doi:10.1029/2003JA010176.

Fomichev, V. I., J. P. Blanchet, and D. S. Turner (1998), Matrix parameterization of the 15 μm CO2 band cooling in the middle and upper atmosphere for variable CO2 concentration, *J. Geophys. Res.*, *103*(D10), 11,505–11,528.

Hedin, A. E. (1991), Extension of the MSIS thermosphere model into the middle and lower atmosphere, *J. Geophys. Res.*, *96*(A2), 1159–1172.

Hoyt, D. V., and K. H. Schatten (1998a), Group sunspot numbers: A new solar activity reconstruction, part 1, *Sol. Phys.*, *179*, 189–219.

Hoyt, D. V., and K. H. Schatten (1998b), Group sunspot numbers: A new solar activity reconstruction, part 2, *Sol. Phys.*, *181*, 491–512.

Hunten, D. M. (1973), The escape of light gases from planetary atmospheres, *J. Atmos. Sci.*, *30*, 1481–1494.

Lean, J. L., O. R. White, W. C. Livingston, and J. M. Picone (2001), Variability of a composite chromospheric irradiance index during the 11-year activity cycle and over longer time periods, *J. Geophys. Res.*, *106*(A6), 10,645–10,658.

Lean, J. L., H. P. Warren, J. T. Mariska, and J. Bishop (2003), A new model of solar EUV irradiance variability: 2. Comparisons with empirical models and observations and implications for space weather, *J. Geophys. Res.*, *108*(A2), 1059, doi:10.1029/2001JA009238.

Liu, J. Y., Y. I. Chen, and J. S. Lin (2003), Statistical investigation of the saturation effect in the ionospheric foF2 versus sunspot, solar radio noise, and solar EUV radiation, *J. Geophys. Res.*, *108*(A2), 1067, doi:10.1029/2001JA007543.

Liu, L., W. Wan, and B. Ning (2004), Statistical modeling of ionospheric foF2 over Wuhan, *Radio Sci.*, *39*, RS2013, doi:10.1029/2003RS003005.

Lobzin, V. V., and A. V. Pavlov (2002), G condition in the F2 region peak electron density: A statistical study, *Ann. Geophys.*, *20*, 523–537.

MacDonald, G. J. F. (1963), The escape of helium from the Earth's atmosphere, *Rev. Geophys.*, *1*, 305–349.

Michel, F. C. (1971), Solar wind induced mass loss from magnetic field-free planets, *Planet. Space Sci.*, *19*, 1580–1583.

Nicolet, M. (1957), The aeronomic problem of helium, *Ann. Geophys.*, *13*, 1.

Norton, R. B. (1969), The middle-latitude F-region during some severe ionospheric storms, *Proc. IEEE*, *57*, 1147–1149.

Pavlov, A. V., and M. J. Buonsanto (1998), Anomalous electron density events in the quiet summer ionosphere at solar minimum over Millstone Hill, *Ann. Geophys.*, *16*, 460–469.

Piggott, W. R., and K. Rawer (1978), *URSI Handbook of Ionogram Interpretation and Reduction*, NOAA, Boulder, Colo.

Radick, R. R. (2003), Variability of sunlike stars, *J. Atmos. Terr. Phys.*, *65*, 105–112.

Radick, R. R., G. W. Lockwood, B. A. Skiff, and S. L. Baliunas (1998), Patterns of variation among Sun-like stars, *Astrophys. J. Suppl. Ser.*, *118*, 239–258.

Ratcliffe, J. A. (1972), *An Introduction to the Ionosphere and Magnetosphere*, Cambridge Univ. Press, New York.

Richards, P. G. (2001), Seasonal and solar cycle variations of the ionospheric peak electron density: Comparison of measurement and models, *J. Geophys. Res.*, *106*(A7), 12,803–12,819.

Richards, P. G., D. G. Torr, and M. R. Torr (1981), Photodissociation of N2: A significant source of thermospheric atomic nitrogen, *J. Geophys. Res.*, *86*(A3), 1495–1498.

Richards, P. G., J. A. Fennelly, and D. G. Torr (1994), EUVAC: A solar EUV flux model for aeronomic calculations, *J. Geophys. Res.*, *99*(A5), 8981–8992.

Rishbeth, H. (1990), A greenhouse effect in the ionosphere?, *Planet. Space Sci.*, *38*, 945–948.

Rishbeth, H., and R. Edwards (1989), The isobaric F2-layer, *J. Atmos. Terr. Phys.*, *51*, 321–338.

Roble, R. G. (1995), Energetics of the mesosphere and thermosphere, in *The Upper Mesosphere and Lower Thermosphere: A Review of Experiment and Theory*, *Geophys. Monogr. Ser.*, vol. 87, edited by R. M. Johnson and T. L. Killeen, pp. 1–21, AGU, Washington, D. C.

Roble, R. G., and R. E. Dickinson (1989), How will changes in carbon dioxide and methane modify the mean structure of the mesosphere and thermosphere?, *Geophys. Res. Lett.*, *16*, 1441–1444.

Roble, R. G., and B. A. Emery (1983), On the global mean temperature of the thermosphere, *Planet. Space Sci.*, *31*(6), 597–614.

Roble, R. G., E. C. Ridley, and R. E. Dickinson (1987), On the global mean structure of the thermosphere, *J. Geophys. Res.*, *92*(A8), 8745–8758.

Schunk, R. W. (1988), A mathematical model of the middle and high latitude ionosphere, *Pure Appl. Geophys.*, *127*, 255–303.

Sethi, N. K., M. K. Goel, and K. K. Mahajan (2002), Solar cycle variations of foF2 from IGY to 1990, *Ann. Geophys.*, *20*, 1677–1685.

Sheldon, W. R., and J. W. Kern (1972), Atmospheric helium and geomagnetic field reversals, *J. Geophys. Res.*, *77*(31), 6194–6201.

Smithtro, C. G. (2004), Response of the ionosphere and thermosphere to extreme solar conditions, Ph.D. dissertation, Utah State Univ., Logan.

Smithtro, C. G., and J. J. Sojka (2005), A new global average model of the coupled thermosphere and ionosphere, *J. Geophys. Res.*, *110*, A08305, doi:10.1029/2004JA010781.

Solanki, S. K., I. G. Usoskin, B. Kromer, M. Schüssler, and J. Beer (2004), Unusual activity of the Sun during recent decades compared to the previous 11,000 years, *Nature*, *431*, 1084–1087, doi:10.1038/nature02995.

St.-Maurice, J.-P., and D. G. Torr (1978), Nonthermal rate coefficients in the ionosphere: The reactions of O+ with N2, O2, and NO, *J. Geophys. Res.*, *83*(A3), 969–977.

Stolarski, R. S. (1976), Energetics of the midlatitude thermosphere, *J. Atmos. Terr. Phys.*, *38*, 863–868.

Tobiska, W. K., T. Woods, F. Eparvier, R. Viereck, L. Floyd, D. Bouwer, G. Rottman, and O. R. White (2000), The SOLAR2000 empirical solar irradiance model and forecast tool, *J. Atmos. Terr. Phys.*, *62*, 1233–1250.

Trinks, H., and K. H. Fricke (1978), Carbon dioxide concentrations in the lower thermosphere, *J. Geophys. Res.*, *83*(A8), 3883–3886.

Upadhyay, H. O., and K. K. Mahajan (1998), Atmospheric greenhouse effect and ionospheric trends, *Geophys. Res. Lett.*, *25*, 3375–3378.

Usoskin, I. G., K. Mursula, and G. A. Kovaltsov (2001), Was one sunspot cycle lost in late XVIII century?, *Astron. Astrophys.*, *370*, L31–L34, doi:10.1051/0004-6361:20010319.

Warren, H. P., J. T. Mariska, and J. Lean (2001), A new model of solar EUV irradiance variability: 1. Model formulation, *J. Geophys. Res.*, *106*(A8), 15,745–15,757.

Webber, W. R., and P. R. Higbie (2003), Production of cosmogenic Be nuclei in the Earth's atmosphere by cosmic rays: Its dependence on solar modulation and the interstellar cosmic ray spectrum, *J. Geophys. Res.*, *108*(A9), 1355, doi:10.1029/2003JA009863.

White, O. R., A. Skumanich, J. Lean, W. C. Livingston, and S. L. Keil (1992), The Sun in a non-cycling state, *Publ. Astron. Soc. Pac.*, *104*, 1139–1143.

Wittmann, A. D., and Z. T. Xu (1987), A catalogue of sunspot observations from 165 BC to AD 1684, *Astron. Astrophys. Suppl. Ser.*, *70*, 83–94.

Woods, T. N., and G. J. Rottman (2002), Solar ultraviolet variability over time periods of aeronomic interest, in *Atmospheres in the Solar System: Comparative Aeronomy*, *Geophys. Monogr. Ser.*, vol. 130, edited by M. Mendillo et al., pp. 221–233, AGU, Washington, D. C.

C. G. Smithtro, Air Force Institute of Technology, Wright-Patterson AFB, OH 45433-7765, USA. (christopher.smithtro@afit.edu)

J. J. Sojka, Center for Atmospheric and Space Sciences, Utah State University, Logan, UT 84322-4405, USA.